Corrosion behavior of Fe–Cr–Ni based alloys exposed to molten MgCl$_2$–KCl–NaCl salt with over-added Mg corrosion inhibitor

Rui Yu[1,2*], **Qing Gong**[3*], **Hao Shi** (✉)[1], **Yan Chai**[3], **Alexander Bonk**[3], **Alfons Weisenburger**[1], **Dihua Wang**[2], **Georg Müller**[1], **Thomas Bauer**[4], **Wenjin Ding** (✉)[3]

1 Institute for Pulsed Power and Microwave Technology, Karlsruhe Institute of Technology (KIT), 76344 Eggenstein-Leopoldshafen, Germany
2 School of Resources and Environmental Science, Wuhan University (WHU), Wuhan 430072, China
3 Institute of Engineering Thermodynamics, German Aerospace Center (DLR), 70569 Stuttgart, Germany
4 Institute of Engineering Thermodynamics, German Aerospace Center (DLR), 70569 Cologne, Germany

Abstract MgCl$_2$–NaCl–KCl salts mixture shows great potential as a high-temperature (> 700 °C) thermal energy storage material in next-generation concentrated solar power plants. Adding Mg into molten MgCl$_2$–NaCl–KCl salt as a corrosion inhibitor is one of the most effective and cost-effective methods to mitigate the molten salt corrosion of commercial Fe–Cr–Ni alloys. However, it is found in this work that both stainless steel 310 and Incoloy 800H samples were severely corroded after 500 h immersion test at 700 °C when the alloy samples directly contacted with the over-added Mg in the liquid form. The corrosion attack is different from the classical impurity-driven corrosion in molten chloride salts found in previous work. Microscopic analysis indicates that Ni preferentially leaches out of alloy matrix due to the tendency to form MgNi$_2$/Mg$_2$Ni compounds. The Ni-depletion leads to the formation of a porous corrosion layer on both alloys, with the thickness around 204 μm (stainless steel 310) and 1300 μm (Incoloy 800H), respectively. These results suggest that direct contact of liquid Mg with Ni-containing alloys should be avoided during using Mg as a corrosion inhibitor for MgCl$_2$–NaCl–KCl or other chlorides for high temperature heat storage and transfer.

Keywords concentrated solar power (CSP), Mg corrosion inhibitor, Mg–Ni intermetallic, salt purification, thermal energy storage (TES)

E-mails: h.shi@mpie.de (Shi H.), wenjin.ding@dlr.de (Ding W.)

* These authors contributed equally to this work.

1 Introduction

Concentrated solar power (CSP) plants are gaining popularity due to their potential to generate dispatchable clean electricity with the help of cost-effective thermal energy storage (TES) [1–4]. In commercial CSP plants, TES materials are typically molten nitrate/nitrite salt with operating temperature below 565 °C to avoid thermal decomposition [4–8]. However, to achieve higher efficiency by integrating with, e.g., a supercritical carbon dioxide (sCO$_2$) Brayton power cycle, a TES material capable of operating at temperatures above 700 °C is required [1]. The adoption of the sCO$_2$ Brayton power cycle in the next generation of CSP plants is expected to achieve a thermal conversion efficiency of over 50%, surpassing the efficiency of conventional Rankine steam cycles used in commercial CSP plants (< 40%), and to significantly reduce the levelized cost of electricity of the CSP plants [1,2,9]. Among the various molten salt candidates, MgCl$_2$–NaCl–KCl salt mixture stands out as a highly promising option due to its low cost (approximately 0.22 USD·kg^{-1} [6]), abundance, low melting temperature (around 385 °C [10]), and low vapor pressure at high temperatures (around 1 kPa at 800 °C [10,11]). However, addressing the compatibility issue (i.e., corrosion) with structural materials, e.g., commercial Fe–Cr–Ni alloys, when exposed to molten MgCl$_2$–NaCl–KCl at temperatures above 700 °C, remains a significant challenge [12–18].

The hygroscopic nature of MgCl$_2$ often results in the formation of salt hydrates, e.g., by absorbing moisture from the surrounding atmosphere [12,16,19]. At elevated temperatures, the reactions (as shown in Eq. (1)) between

the chloride and water can generate corrosive species, such as HCl and MgOHCl [16,19–21]. The typical degradation mechanism observed in Fe–Cr–Ni alloys immersed in molten chlorides involves the preferential depletion of Cr. This depletion primarily occurs due to reactions with corrosive impurities in the molten chlorides such as MgOHCl. Equation (2) shows the reaction of Cr with MgOHCl [12,16,20].

Several corrosion mitigation strategies have been explored, including thermal salt purification [10,22], chemical salt purification through the addition of corrosion inhibitors [14,23–29], carbon-chlorination [30], and electrochemical purification by electrolysis of corrosive impurities [31,32]. One particularly effective and cost-effective approach is the addition of Mg as a corrosion inhibitor [14,15,22,28,29,33]. The corrosion mitigation mechanism of adding Mg is to lower the redox potential of salts by reducing the corrosive impurities such as MgOHCl (see Eq. (3)) [12,14–16,22,28,29]. For instance, the addition of 2.8 wt % Mg in the $MgCl_2$–NaCl–KCl mixture has demonstrated a significantly reduction in the corrosion rates of commercial Fe-based alloys, such as SS 310 and In 800H, to below than 15 $\mu m \cdot a^{-1}$ at 700 °C in our previous work [29]. By employing low-cost stainless steels as the main structural materials for the hot salt tank, rather than much more expensive Ni-based alloys, a TES system can be achieved with a capital expenditure of approximately 27 $\cdot kWh$-th^{-1}, which is comparable to commercial TES system with molten nitrates (20–33 $\cdot kWh$-th^{-1}) [29].

$$MgCl_2 + H_2O \rightarrow MgOHCl(s,l) + HCl(g) \qquad (1)$$

$$Cr + 2MgOHCl \rightarrow 2MgO + CrCl_2(s,l,g) + H_2(g) \qquad (2)$$

$$Mg + 2MgOHCl \rightarrow 2MgO + MgCl_2(s,l) + H_2(g) \qquad (3)$$
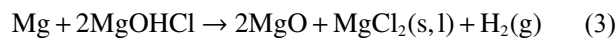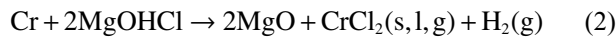
Due to the lower electromotive force (EMF) of Ni (0.88 V at 800 °C) compared to Cr (1.35 V at 800 °C) and Fe (1.12 V at 800 °C) in molten chlorides [16,27,34], Ni exhibits better corrosion resistance in molten chlorides as discussed in open literature [10,13,16,17,35,36]. Our previous research has shown that the corrosion inhibitor Mg (EMF: 2.46 V at 800 °C [27]) can effectively reduce the corrosion rates of Fe–Cr–Ni alloys when immersed in molten chloride salt with corrosive impurities like $MgOH^+$ [29]. However, in the same study [29], a Ni-rich layer with a thickness of 20 μm was observed on In 800H sample, while some Ni pieces formed on SS 310, after 2000 h of immersion in the Mg-rich molten chloride salt solution. This Ni enrichment could be attributed to the formation of Mg–Ni intermetallic compounds (IMCs),

such as Mg_2Ni and $MgNi_2$ [23–26]. The formation of Mg–Ni compounds at high temperature has been discussed in other fields, including material processing [37–40] and electrolysis [41]. Some previous studies have reported instances of over-added Mg-induced corrosion in molten chloride salt [23–26]. However, these studies are often complicated by the typical $MgOH^+$-driven corrosion. The over-added Mg-induced corrosion was considered a secondary cause of corrosion, and its corrosion mechanism was not thoroughly investigated.

In this study, two commercial Fe-based alloys SS 310 and In 800H, with different Ni contents, were exposed to molten $MgCl_2$–KCl–NaCl with over-added Mg at 700 °C for 500 h in an inert atmosphere. To reduce the interference of $MgOH^+$-driven corrosion, the molten chloride salt was purified through over-added Mg, as described in previous methods [29]. Samples that were in contact and not in contact with Mg were obtained from the exposure tests for comparative analysis. The surfaces and cross-sections of the exposed samples were examined using scanning electron microscopy (SEM) and energy-dispersive X-ray spectroscopy (EDX). The discussion focused on the effect of contact with liquid Mg on the alloy samples.

2 Experimental

2.1 Chemicals and alloys

Each corrosion test utilized approximately 50 g of anhydrous $MgCl_2$–NaCl–KCl mixtures (47.1/30.2/22.7 mol %, purity > 99 wt %, Alfa Aesar). Due to the short exposure in air, the salt mixture contains a small amount of hydrated water (about 1 wt %) [29]. Magnesium metal bars (purity > 99%) with 5 mm diameter were polished to remove the surface oxides and used as the corrosion inhibitor in the immersion test. Table 1 provides a summary of the chemical compositions of two commercially Fe-based alloys containing Ni (SS 310 and In 800H), which were employed in this work [16]. Prior to immersion, the SS 310 sample (20 mm × 10 mm × 2 mm) and In 800H sample (20 mm × 10 mm × 2 mm) underwent grinding by 1200 grit sandpapers, followed by ultrasonically washing in distilled water and acetone to achieve a smooth and clean surface.

2.2 Immersion tests

The experimental setup and photos of In 800H samples

Table 1 Chemical compositions (main alloying elements) of the studied alloys (wt %)[a)]

Alloy	Fe	Ni	Cr	C	Mn	Si	P	S	Al	Ti
SS 310	Bal.	19–22	24–26	0.25	2	1.75	0.045	0.030	–	–
In 800H	Bal.	30–35	19–23	0.05–0.07	1.50	1.00	0.045	0.015	0.15–0.60	0.15–0.60

a) Data source: website of Sandmeyer Steel Company, accessed on January 29, 2023.

are illustrated in Fig. 1. As shown in Fig. 1(a), an alumina crucible containing 50 g mixture of $MgCl_2$–NaCl–KCl with an additional 2.8 wt % Mg was positioned at the bottom of a furnace. The furnace was then heated to 700 °C under an inert atmosphere (Ar purity $\geqslant$ 99.999%, O_2 and H_2O < 1 ppm (1 ppm = 10^{-6}), flow rate: 10 $L\cdot h^{-1}$) for 16 h to purify the molten chlorides with liquid Mg prior to the corrosion test [29]. This purification process reduced the concentration of corrosive impurity (MgOHCl) to less than 200 ppm oxygen (ppm O, by weight < 0.1 wt %) as determined by titration method [12], resulting in significantly reduced corrosiveness of the molten chloride salt. This allowed for a clear examination of the effect of over-added Mg on alloy corrosion.

Following the purification, the alloy pieces were suspended by a nickel wire and fully immersed in the molten chlorides in the crucibles. Crucibles 1 and 2 contained a SS 310 piece and an In 800H piece, respectively, while crucible 3 contained a SS 310 piece. To prevent galvanic coupling, the nickel wires and tested samples were isolated using alumina tubes (for more details refer to our previous work [29]).

After 500 h exposure, the SS 310 and In 800H pieces (Samples 1 and 2) in crucible 1 were quickly lifted out of molten chlorides at 700 °C to avoid contact with and attachment of Mg on its surface (Fig. 1(c)). To study the effects of liquid Mg contact and attachment, the SS 310 piece in crucible 3 (Sample 5) was lifted out of the molten salt at 700 °C with attached Mg on its surface, achieved by providing more contact time between the alloy and the liquid Mg metal floating on the molten salt. Subsequently, the furnace was cooled to room temperature in Ar atmosphere over a 10-h period. The SS 310 and In 800H pieces in crucible 2 (Samples 3 and 4) were obtained from the solidified salt after cooling to
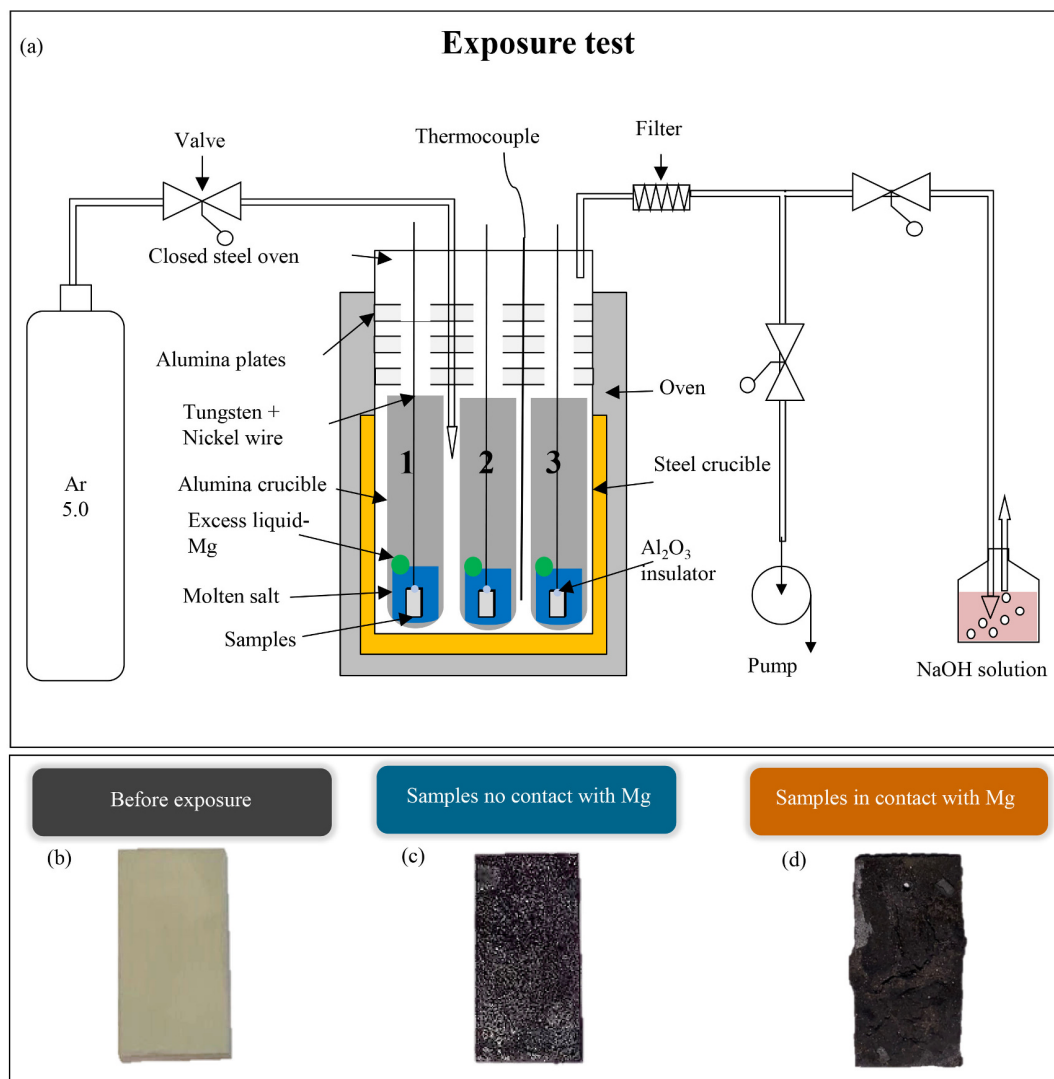
Fig. 1 (a) Schematic diagram of experimental set-up for immersion tests. (b–d) Photos of In 800H samples obtained under different conditions. (b) Before exposure, (c) extracted sample without contact with Mg (Sample 2), (d) extracted samples in contact with Mg after salt cooling (Sample 4), sample in contact with liquid Mg when lifting out (Sample 5).

room temperature (about 16 h). Upon observation after washing with distilled water, it was determined that these samples came into contact with Mg (Fig. 1(d)).

Table 2 provides a list of the samples with different test conditions. By comparing Sample 1 (without Mg contact) with Sample 5, the effect of liquid Mg contact and attachment was investigated. Additionally, the comparison between Samples 1 and 2 (without Mg contact) and Samples 3 and 4 (with Mg contact due to salt cooling) aimed to examine the effect of potential Mg solidification in the cold parts of the molten chloride TES system (420–800 °C) such as the cold tank, as Mg has a melting temperature of approximately 650 °C.

2.3 Microstructure analysis

After exposure, the samples were cleaned using distilled water to eliminate any remaining salt deposits. Subsequently, they were dried and sealed in an airtight manner to maintain their condition. To analyze the cross-section and surface morphology of the samples, scanning electron microscope (Zeiss LEO 1530 VP) equipped with

EDX was used for microstructure characterization. The electron beam energy varies in the range of 10 to 20 keV with a working distance of 9 mm.

3 Results and discussion

3.1 Results

Figures 1(c) and 1(d) show surface images of In 800H samples extracted from molten salts using different methods outlined in Table 2. In comparison to the original In 800H (Fig. 1(b)), Sample 2 lifted out of the molten salt at 700 °C without contact with liquid Mg was covered only with a dark MgO layer without any presence of Mg (Fig. 1(c)). However, Sample 4, extracted at room temperature, displayed the presence of Mg pieces on its surface (over-added Mg).

Figure 2 shows the SEM-EDX cross-section analysis of SS 310 and In 800H (Samples 1 and 2) lifted out at 700 °C without any surface contamination from Mg. Our previous work showed that the molten salts had a low

Table 2 Sample parameters and experimental conditions used for the corrosion tests

Sample code	Type	Sample size/mm^3	Crucible	Duration of immersion hours in molten salt	Sampling method	Contact with high-temperature Mg (contact time)
Sample 1	SS 310	$10 \times 10 \times 2$	1	500	Lifted out of the molten salt at 700 °C	No
Sample 2	In 800H	$20 \times 10 \times 2$	1	500	Lifted out of the molten salt at 700 °C	No
Sample 3	SS 310	$10 \times 10 \times 2$	2	500	Sampling from solid salt at room temperature	Yes (cooling time)
Sample 4	In 800H	$20 \times 10 \times 2$	2	500	Sampling from solid salt at room temperature	Yes (cooling time)
Sample 5	SS 310	$20 \times 10 \times 2$	3	500	Lifted out of the molten salt at 700 °C	Yes (lifting-out time)
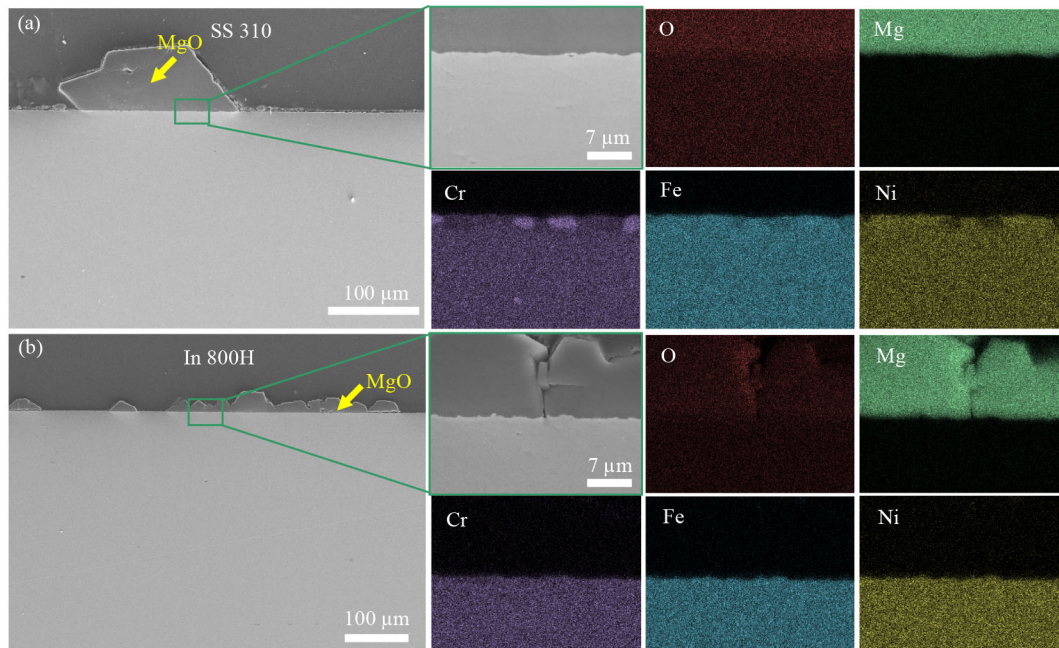
Fig. 2 SEM images and EDX elemental mappings of cross section of (a) SS 310 (Sample 1) and (b) In 800H (Sample 2) lifted out at 700 °C without contact with liquid Mg, after 500 h immersion in molten MgCl$_2$–KCl–NaCl with 2.8 wt % Mg addition.

concentration of impurities (< 0.1 wt %, MgOHCl) because of the salt purification and continuous protection by the over-added Mg [29]. As a result, both Sample 1 and Sample 2 exhibited minimal corrosion, with only a few MgO precipitates covering the alloy surface. No depletion of Cr, Fe, or Ni was detected in the bulk material, as observed in Figs. 2(a) and 2(b). Furthermore, The EDX elemental mapping of SS 310 (Sample 1) revealed an enrichment of Cr in certain regions near the interface of MgO precipitates and the bulk material, as depicted in Fig. 2(a). This enrichment could be attributed to formation of Cr-rich compounds at 700 °C after 500 h exposure, as described in the literature [29,42,43]. No corrosion attack or depletion of elements was observed in both samples. The aforementioned results indicate that both SS 310 and In 800H demonstrate good corrosion resistance when exposed to molten MgCl$_2$–KCl–NaCl salt at 700 °C that has been purified with Mg, consisting with our previous research [29].

Figure 3 depicts the cross-sectional SEM image and EDX elemental mapping of SS 310 (Sample 3) obtained by cooling down to room temperature. A discernible layer comprising of Ni, Mg, and O elements is observable on the surface of the metal sample. Beneath the surface layer, a porous corrosion layer with a thickness of approximately 204 μm is observed due to contact with Mg during cooling process. The distribution of Ni suggests the presence of a Ni-depleted layer beneath the alloy surface, while the distribution of Cr and iron Fe remains unchanged except within the pores. Figure 4 presents the EDX line scanning results of the cross section of SS 310. In Fig. 4(a), the enlarged SEM image reveals that the corrosion layer consists of numerous islands. These islands exhibit enrichment of both Mg and Ni, indicating the formation of Mg–Ni IMCs in the corroded layer (Fig. 4(b)). The line scan analysis confirms a decrease in Ni content to approximately 7 wt % in the porous corrosion layer, while the contents
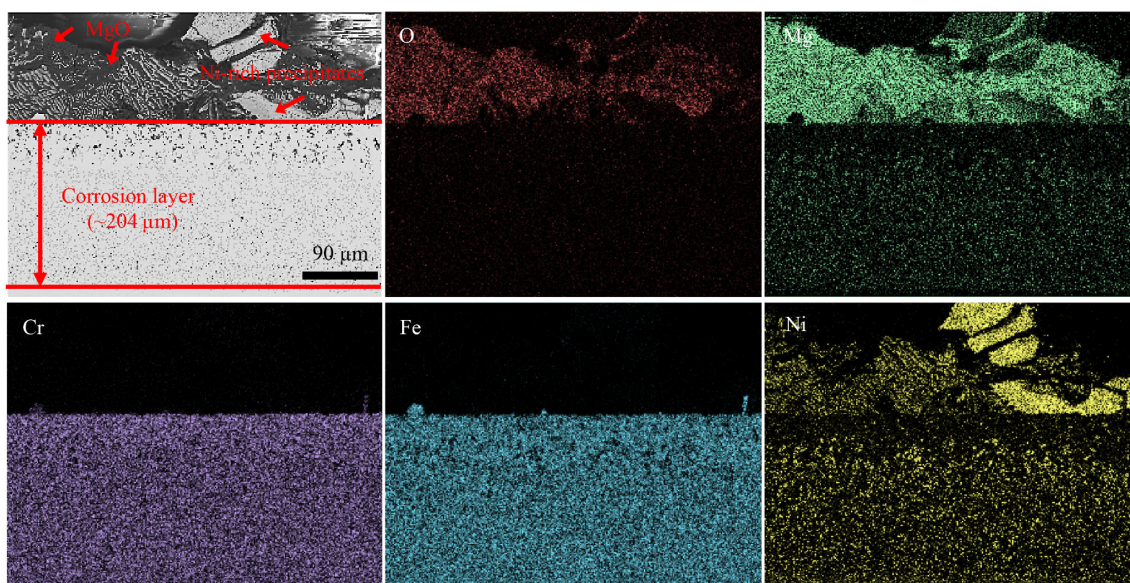
Fig. 3 SEM image and EDX elemental mapping of the cross section of SS 310 (Sample 3) extracted at room temperature after cooling-down of the molten MgCl$_2$–KCl–NaCl with 2.8 wt % Mg addition after 500 h immersion test.
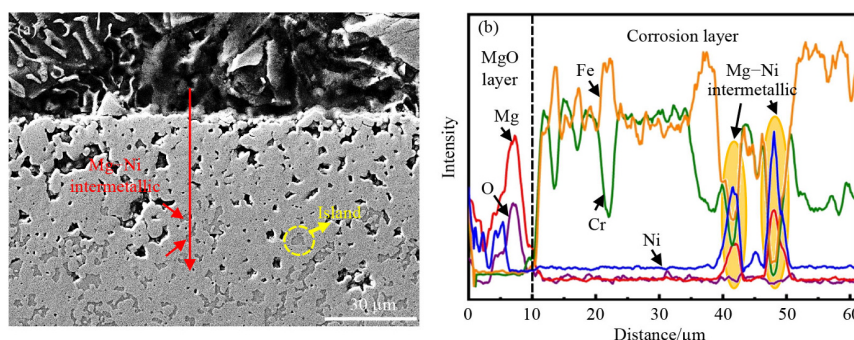
Fig. 4 (a) Enlarged SEM image and (b) EDX line scanning profile of the cross section of SS 310 (Sample 3) extracted at room temperature after cooling-down of the molten MgCl$_2$–KCl–NaCl with 2.8 wt % Mg addition after 500 h immersion test. The islands marked on the SEM picture are Mg–Ni-rich phases, Mg–Ni IMCs.

of Cr and Fe remain at approximately 25 and 50 wt %, respectively, maintaining the same levels in the matrix.

Figure 5 illustrates the cross-section SEM image of In 800H (Sample 4) extracted at room temperature after cooling down under Ar atmosphere. The surface of the alloy is covered by an MgO layer with dispersed Ni and Ni-rich precipitates (Fig. 5(a)). Notably, a corrosion layer with a thickness of approximately 1300 μm (long contact time with high-temperature Mg during cooling down) is observed, which is significantly greater than that of Sample 3 (~200 μm in SS 310). This contradicts the conventional understanding that alloys with higher Ni content have better corrosion resistance in molten chloride salt [16]. Furthermore, the thickness of the corrosion layer in this work exceeds that of typical Cr-depletion corrosion in the molten $MgCl_2$–KCl–NaCl salt without Mg addition after being immersed to 700 °C for 500 h (~50 μm [16]). In Fig. 5(b), the EDX elemental mapping of the sample reveals a thick surface layer primarily composed of Mg and Ni. The underlying Ni shows significant depletion, with the remaining Ni is consistently associated with the Mg signal at the grain boundaries (GBs). This observation suggests the

formation and retention of Mg–Ni IMCs in the corrosion layer at the GBs. This is further supported by the EDX line scan in Fig. 5(c), which demonstrates Ni depletion in the internal corrosion layer.

In Fig. 6, SEM images of Sample 5 (SS 310) are presented, which was lifted out of molten salt at 700 °C and came into contact with and attachment of liquid Mg. Upon cooling for a few minutes in the upper part of the furnace, the Mg ingot solidified on the surface of SS 310, as the melting temperature of Mg is about 650 °C. The inset digital image in Fig. 6(b) depicts the solidified Mg shell (visible as dark contrast) on the surface of sample. Further cross-sectional analysis of the region covered by Mg reveals severe corrosion of the alloy, characterized by a corrosion layer with 120 μm thickness when contact time with high-temperature Mg < 10 min (as shown in Fig. 6(a)). In contrast, the surface area without the Mg shell or covered by only a few Mg droplets shows less corrosion, with a maximum corroded layer of 40 μm (as shown in Fig. 6(b)). This result provides additional support to the notion that corrosion observed in Figs. 3–5 is driven by Mg–Ni reactions, rather than by the molten salt. It also indicates that corrosion induced by Mg–Ni
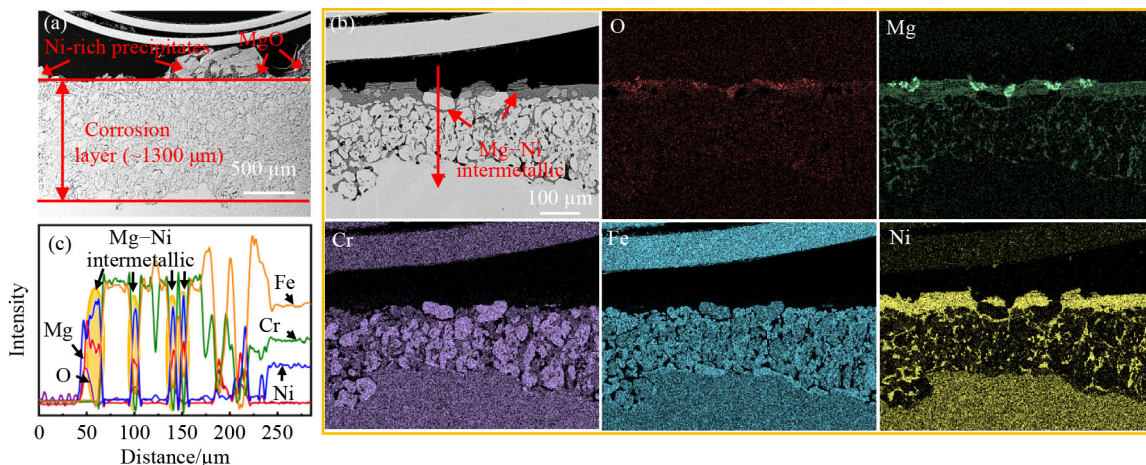
Fig. 5 (a) SEM image, (b) the backscattered electron image and EDX elemental mapping, and (c) EDX line scanning profiles of cross section of In 800H (Sample 4) extracted at room temperature after cooling-down of the molten $MgCl_2$–KCl–NaCl with 2.8 wt % Mg addition after 500 h immersion test.
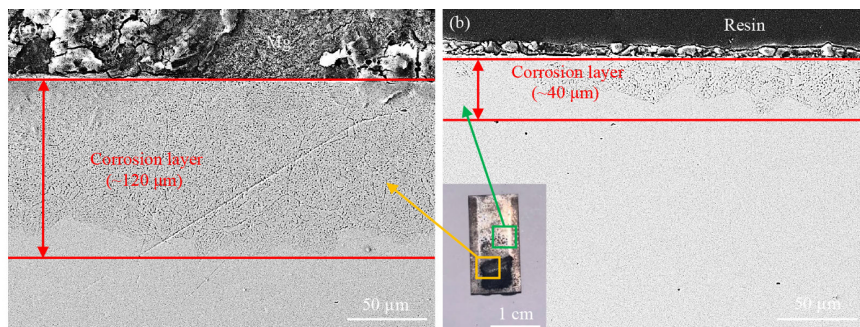
Fig. 6 SEM images of cross section of SS 310 (Sample 5) with Mg adhered to the surface. (a) The area completely covered by Mg ingot, (b) the area contacted with some Mg droplets. The inset graph: digital photos of SS 310 with Mg ingot adhesion.

alloying is significantly faster than corrosion driven by impurities present in the molten salt.

Figure 7 displays a detailed analysis of the Mg-covered region on the surface of Sample 5. The surface analysis, shown in Fig. 7(a), reveals the presence polygonal flakes enriched with Mg and Ni, in addition to the MgO particles. This observation confirms the formation of Mg–Ni IMCs in the corrosion layer. The cross-section analysis in Fig. 7(b) indicates that Mg and Ni are the dominant elements in the surface layer. Below this layer, a porous polygonal corrosion area is observed, which is characterized by a depletion of Ni. This depletion is attributed to the outward leaching of Ni from the alloy structure.

By comparing Sample 1 (without Mg contact) with Sample 5, it can be concluded that liquid Mg exhibits high corrosiveness toward the Ni-containing alloys. Therefore, direct contact between liquid Mg with the Ni-containing alloys should be avoided to prevent such

corrosion. Moreover, comparing Samples 1 and 2 (without Mg contact) with Samples 3 and 4 (contact with Mg due to salt cooling) indicates that Mg has high corrosivity to the commercial Ni–Fe–Cr alloys when close to its melting temperature. Consequently, special attention should be given to the potential over-adding of Mg and its solidification in the cold region of a molten chloride TES system, such as the cold tank.

3.2 Discussion

3.2.1 Corrosion mechanism of Fe–Cr–Ni alloys with Mg in molten chloride salt

Figure 8 presents a comparison of the densities of Mg metal and molten $MgCl_2$–KCl–NaCl as a function of temperature ranging from 400 to 700 °C. The graph shows that the density of $MgCl_2$–KCl–NaCl is similar to that of liquid Mg at 700 °C, indicating that liquid Mg can
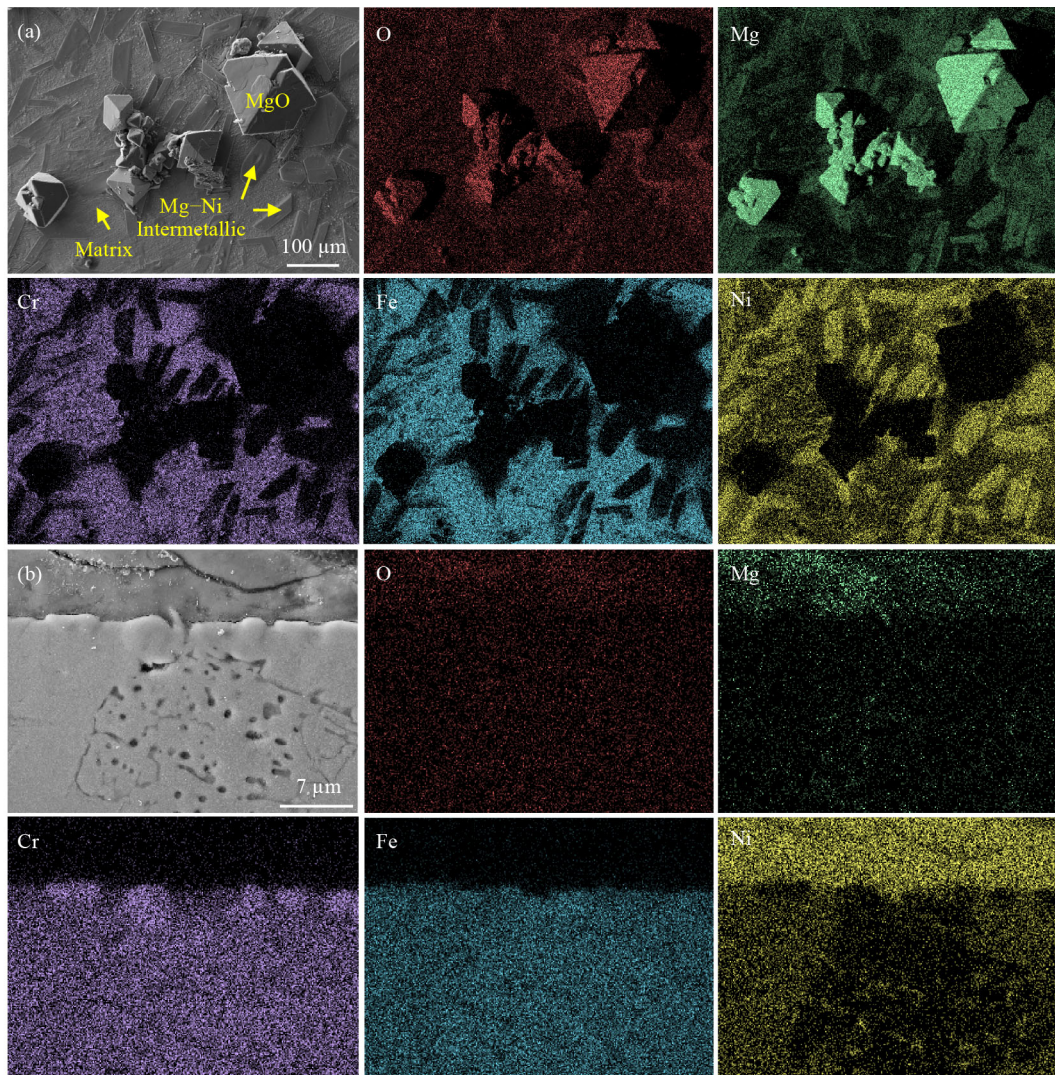
Fig. 7   SEM images and EDX elemental mapping of (a) surface morphology and (b) cross section of SS 310 (Sample 5) extracted at 700 °C by lifting-out, which has Mg droplets on the surface.
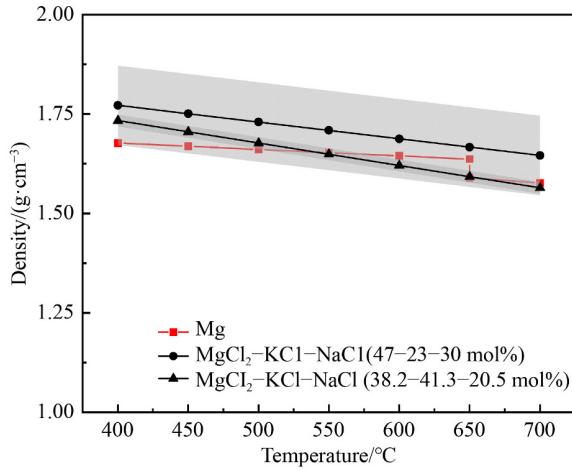
Fig. 8 Densities of Mg [44,45] and MgCl$_2$–KCl–NaCl [11,46] in the temperature range of 400–700 °C. The shaded areas indicate the errors.

float or be suspended in the molten salts. This observation was experimentally confirmed by successfully sampling the Mg metal floating on the molten salt at 700 °C in this work.

When the liquid Mg metal comes into directly contact with alloy at the surface, it increases the susceptibility of Ni loss, leading to a higher corrosion rate of the alloy.

This effect is evident in the analysis of Sample 5, which was lifted out of the molten chloride salt and had contact with liquid Mg on the surface for <10 min. Upon cooling the salt to room temperature, the solid Mg could settle to the bottom of the crucible or suspend in the molten salt due to significantly increased density upon solidification (Fig. 8). Consequently, this could lead to the contact of the alloy samples immersed in the molten salt with the high-temperature (close to melting temperature of 650 °C) Mg, resulting in severe corrosion of the alloy samples, as observed in Samples 3 and 4.

Figure 9 shows the phase diagrams of the Mg–Ni system [47], Mg–Fe system [48], and Mg–Cr system [48]. The Mg–Ni phase diagram indicates that when liquid Mg comes into direct contact with a Ni-rich region at elevated temperature (> 508 °C), stable compounds such as Mg$_2$Ni and MgNi$_2$ can form. Due to the negative Gibbs free energy of MgNi$_2$ and Mg$_2$Ni, Ni in bulk alloy is attracted and leached out. On the other hand, the phase diagrams of the Mg–Fe and Mg–Cr systems, as shown in Figs. 9(b) and 9(c), respectively, reveal that no stable metallic compound phases are maintained in these systems.

$$\text{Mg} + 2\text{Ni} = \text{MgNi}_2 \quad \Delta G_{700\,°C} = -46.01 \text{ kJ} \cdot \text{mol}^{-1} \quad (4)$$
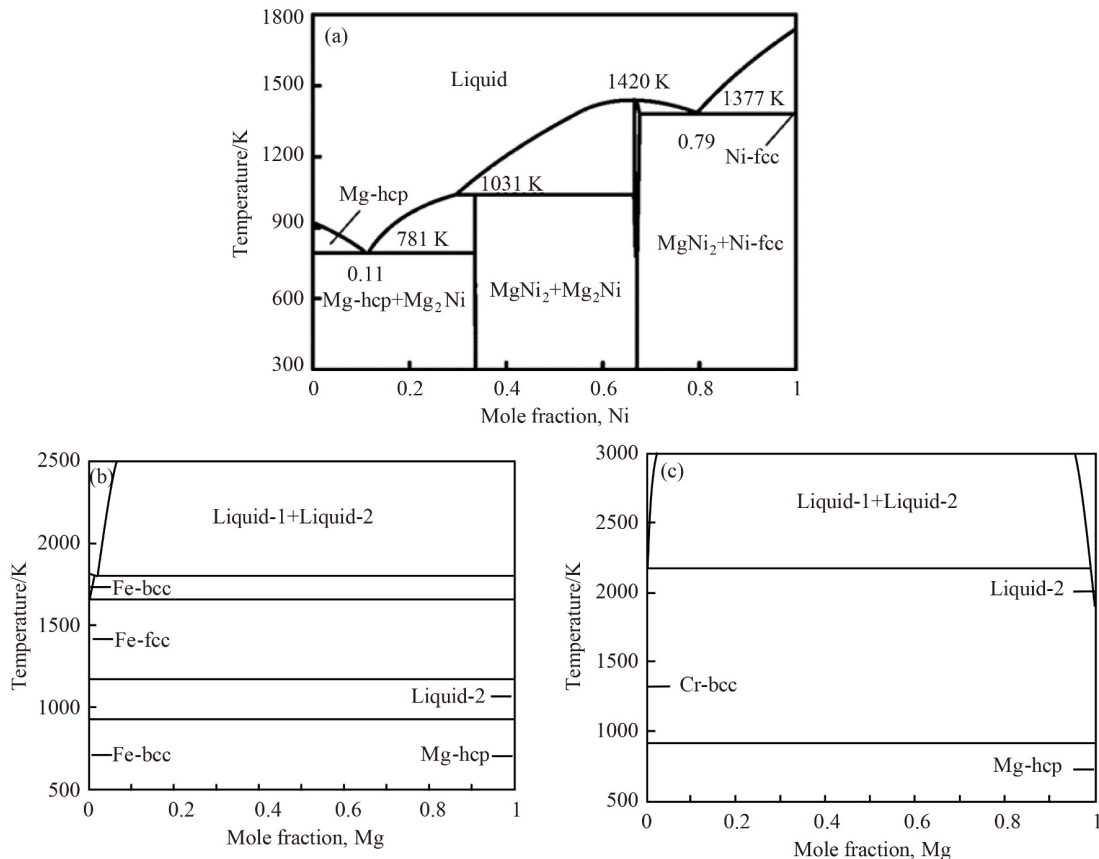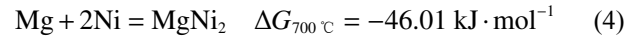
Fig. 9 Phase diagrams of (a) Mg–Ni system [47], (b) Mg–Fe system [48], and (c) Mg–Cr system [48] (fcc: facedcenteredcubic, bcc: body-centered cubic, hcp: hexagonal close-packed).

$$2Mg + Ni = Mg_2Ni \quad \Delta G_{700\,°C} = -29.02\ kJ \cdot mol^{-1} \quad (5)$$
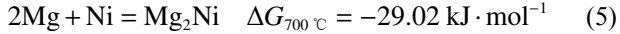
In this study, 1.4 g of Mg (2.8 wt %) was over-added to 50 g of MgCl$_2$–KCl–NaCl to remove the major corrosive impurity (MgOHCl) during pre-purification and immersion testing. In previous work [16,29,49], the initial concentration of MgOHCl in MgCl$_2$–KCl–NaCl was approximately 3000 ppm O. After 16 h of salt purification with Mg, the concentration of MgOHCl was reduced to approximately 200 ppm O [29] due to the full reaction of MgOHCl with liquid Mg at 700 °C. It is estimated that approximately 0.1 g of Mg (equivalent to about 0.2 wt % in the 50 g salt) was consumed during the purification process, leaving about 1.3 g over-added liquid Mg in the melts during the corrosion exposure.

Figure 10 depicts the corrosion mechanism of Ni-containing metallic samples when exposed to molten chlorides with over-added Mg at 700 °C or close to its melting temperature. Upon contact between the liquid or high-temperature solid Mg and SS 310 or In 800H, Mg–Ni IMCs (Mg$_2$Ni and MgNi$_2$) could form simultaneously, as shown in Fig. 10, Eqs. (4) and (5). This phenomenon has been observed and studied by several research groups in the field of metal processing by various research groups [37–40]. The formation of Mg–Ni IMCs can occur rapidly, even within a short contact time between the alloy and liquid Mg. For instance, in a study on the liquid phase bonding of stainless steel to magnesium alloy, where a significant amount of Mg–Ni IMCs formed at 530 °C within 20 min in the AZ-31-Mg-alloy/Ni/SS 316L bond, as indicated by X-ray diffraction spectrum [40]. In the current study, the oxide film on SS 310 and In 800H samples is not dense (as shown in Fig. 2), leaving the bare metal surface directly exposed molten salts to Mg metal. Therefore, the liquid Mg in contact with Ni-containing samples reacts with the bare metal surface immediately, resulting in the immediate formation of Mg–Ni IMCs, as observed in the SEM-EDX images (Figs. 3–7). This explains the alloy containing more Ni (In 800H) corrodes faster than the one with less Ni (SS 310) when exposed to liquid Mg. Since Mg–Ni eutectic has the melting temperature of about 508 °C (Fig. 9(a)), considerable Ni element diffuses out of the alloy matrix by forming Mg$_2$Ni IMCs with liquid Mg and lead to porous morphology in the corrosion layer.

3.2.2 Application of Mg corrosion inhibitor in molten chloride salt system

It is widely accepted that molten chloride salts should be thoroughly pre-treated and purified before use in molten salt reactors [25,33,36] or in TES [2,10,15] at high temperatures (700 °C or above). Additionally, impurity induced corrosion in molten chloride salts should be prevented during operation. Mg is considered to be the most effective purifier and inhibitor for molten MgCl$_2$–KCl–NaCl to remove corrosive impurities such as MgOHCl and to act as a sacrificial anode to protect Fe–Cr–Ni alloys [10,21,25,27,29,33].

There is some literature on the design and implementation of Mg pre-treatment in molten MgCl$_2$–KCl–NaCl [9,28,29,33,50]. Over-added liquid Mg in molten chloride salt increases the contact areas and reaction rates. This leads to an efficient process for large-scale purification (e.g., for TES with thousands of tonnes of salt). However, the over-added Mg-purifier should be severely restricted and prevented from contacting Ni-containing structural materials (e.g., vessel wall) at high temperatures. Otherwise, the Mg-induced corrosion on the Ni-containing vessel would destroy the container rapidly. To avoid this problem, it is suggested to add suitable amount
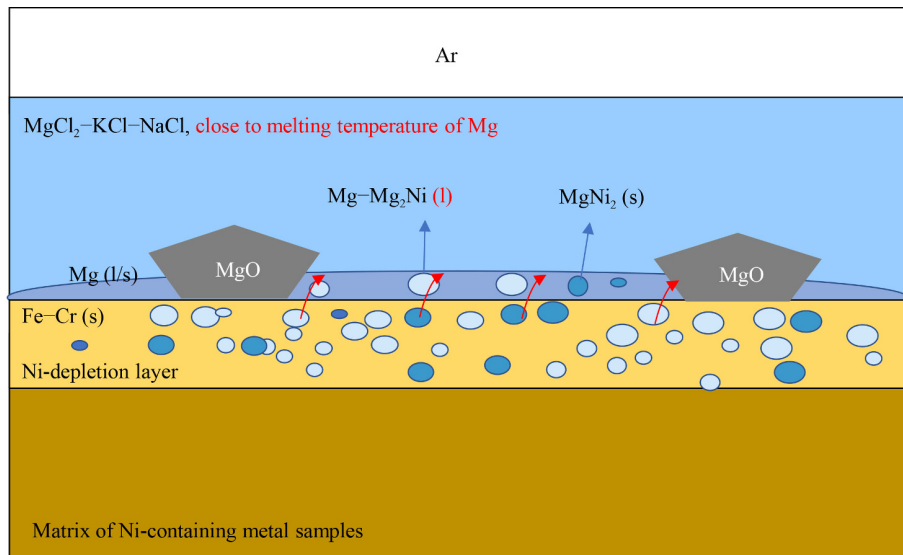
Fig. 10 Schematic illustration of the corrosion mechanism of over-added Mg to Fe–Cr–Ni alloy in molten MgCl$_2$–NaCl–KCl at 700 °C or close to melting temperature of Mg.

of Mg in the molten salt according to the amount of corrosive impurities in the salt or avoid the contact of the high-temperature Mg with the Ni-containing alloys.

4　Conclusions

This work investigated corrosion mechanisms of SS 310 and In 800H caused by Mg in molten $MgCl_2$–KCl–NaCl at 700 °C under an inert atmosphere. After excluding the typical impurity-induced degradation of metallic materials in molten chloride salt, the effect of over-added Mg on corrosion of the two candidate Ni-containing alloys was studied. The main conclusions of Mg-induced corrosion are summarized as following:

1) Both SS 310 and In 800H exhibit severe corrosion attack due to contact with high-temperature Mg in molten $MgCl_2$–KCl–NaCl. The corrosion depth of SS 310 and In 800H reaches to 204 and 1300 μm within 500 h, which are much higher than typical impurity-induced corrosion.

2) The corrosion of the tested alloys in terms of Ni leaching, is driven by the strong affinity between Mg and Ni. SEM-EDX measurements revealed the presence of Mg_2Ni and $MgNi_2$ compounds on the alloy surfaces and within the sample matrix.

3) The remarkably high corrosion rates observed in this work indicate that such direct contact with high-temperature Mg can cause severe damage to Fe–Cr–Ni alloys. Therefore, such contact should be avoided during salt purification and in subsequent facility operation stage.

4) To prevent the over-added Mg corrosion, it is recommended to add an appropriate amount of Mg to the molten salt, taking into account the level of corrosive impurities in the salt, or avoid the contact of the high-temperature Mg with the Ni-containing alloys.

References

1. Mehos M, Turchi C, Vidal J, Wagner M, Ma Z, Ho C, Kolb W, Andraka C, Kruizenga A. Concentrating Solar Power Gen3 Demonstration Roadmap. National Renewable Energy Lab. (NREL), Technical Report, 2017
2. Ding W, Bauer T. Progress in research and development of molten chloride salt technology for next generation concentrated solar power plants. Engineering (Beijing), 2021, 7(3): 334–347
3. IRENA. Renewable Power Generation Costs in 2020. Abu Dhabi: International Renewable Energy Agency, 2021
4. Romero M, González-Aguilar J. Solar thermal CSP technology. Wiley Interdisciplinary Reviews. Energy and Environment, 2014, 3(1): 42–59
5. Nunes V M B, Queirós C S, Lourenço M J V, Santos F J V, Nieto de Castro C A. Molten salts as engineering fluids—a review: Part I. Molten alkali nitrates. Applied Energy, 2016, 183: 603–611
6. Turchi C S, Vidal J, Bauer M. Molten salt power towers operating at 600–650 °C: salt selection and cost benefits. Solar Energy, 2018, 164: 38–46
7. Bonk A, Sau S, Uranga N, Hernaiz M, Bauer T. Advanced heat transfer fluids for direct molten salt line-focusing CSP plants. Progress in Energy and Combustion Science, 2018, 67: 69–87
8. Carrillo A J, González-Aguilar J, Romero M, Coronado J M. Solar energy on demand: a review on high temperature thermochemical heat storage systems and materials. Chemical Reviews, 2019, 119(7): 4777–4816
9. Turchi C, Gage S, Martinek J, Jape S, Armijo K, Coventry J, Pye J, Asselineau C-A, Venn F, Logie W. CSP Gen3: Liquid-Phase Pathway to SunShot. National Renewable Energy Lab. (NREL), Technical Report, 2021
10. Zhao Y. Molten Chloride Thermophysical Properties, Chemical Optimization, and Purification. National Renewable Energy Lab. (NREL), Technical Report, 2020
11. Villada C, Ding W, Bonk A, Bauer T. Engineering molten $MgCl_2$–KCl–NaCl salt for high-temperature thermal energy storage: review on salt properties and corrosion control strategies. Solar Energy Materials and Solar Cells, 2021, 232: 111344
12. Ding W, Bonk A, Bauer T. Corrosion behavior of metallic alloys in molten chloride salts for thermal energy storage in concentrated solar power plants: a review. Frontiers of Chemical Science and Engineering, 2018, 12(3): 564–576
13. Sun H, Wang J, Li Z, Zhang P, Su X. Corrosion behavior of 316SS and Ni-based alloys in a ternary NaCl–KCl–$MgCl_2$ molten salt. Solar Energy, 2018, 171: 320–329
14. Anderson M, Sridharan K, Morgan D, Peterson P, Calderoni P, Scheele R, Casekka A, McNamara B. Heat Transfer Salts for Nuclear Reactor Systems-Chemistry Control, Corrosion Mitigation, and Modeling. University of Wisconsin, Madison, WI; University of California, Berkeley; Pacific Northwest National Lab, Richland, WA. Technical Report, 2015
15. Sun H, Wang J Q, Tang Z, Liu Y, Wang C. Assessment of effects of Mg treatment on corrosivity of molten NaCl–KCl–$MgCl_2$ salt with Raman and infrared spectra. Corrosion Science, 2020, 164: 108350
16. Ding W, Shi H, Xiu Y, Bonk A, Weisenburger A, Jianu A, Bauer T. Hot corrosion behavior of commercial alloys in thermal energy storage material of molten $MgCl_2$/KCl/NaCl under inert atmosphere. Solar Energy Materials and Solar Cells, 2018, 184: 22–30
17. Mortazavi A, Zhao Y, Esmaily M, Allanore A, Vidal J, Birbilis N. High-temperature corrosion of a nickel-based alloy in a molten chloride environment—the effect of thermal and chemical purifications. Solar Energy Materials and Solar Cells, 2022, 236: 111542
18. Mayes R T, Kurley J M, Halstenberg P W, McAlister A,

Sulejmanovic D, Raiman S, Dai S, Pint B. Purification of Chloride Salts for Concentrated Solar Applications. Oak Ridge National Laboratory (ORNL), Technical Report, 2018

19. Kipouros G J, Sadoway D R. A thermochemical analysis of the production of anhydrous $MgCl_2$. Journal of Light Metals, 2001, 1(2): 111–117

20. Grégoire B, Oskay C, Meißner T, Galetz M. Corrosion mechanisms of ferritic-martensitic P91 steel and Inconel 600 nickel-based alloy in molten chlorides. Part II: NaCl–KCl–$MgCl_2$ ternary system. Solar Energy Materials and Solar Cells, 2020, 216: 110675

21. Ren S, Chen Y, Ye X X, Jiang L, Yan S, Liang J, Yang X, Leng B, Li Z, Chen Z, Dai Z. Corrosion behavior of carburized 316 stainless steel in molten chloride salts. Solar Energy, 2021, 223: 1–10

22. Zhao Y, Klammer N, Vidal J. Purification strategy and effect of impurities on corrosivity of dehydrated carnallite for thermal solar applications. RSC Advances, 2019, 9(71): 41664–41671

23. D'Souza B, Zhuo W, Yang Q, Leong A, Zhang J. Impurity driven corrosion behavior of HAYNES® 230® alloy in molten chloride salt. Corrosion Science, 2021, 187: 109483

24. Pint B A, McMurray J W, Willoughby A W, Kurley J M, Pearson S R, Lance M J, Leonard D N, Meyer H M, Jun J, Raiman S S, Mayes R T. Re-establishing the paradigm for evaluating halide salt compatibility to study commercial chloride salts at 600–800 °C. Materials and Corrosion, 2019, 70(8): 1439–1449

25. Pint B. Progression to Compatibility Evaluations in Flowing Molten Salts. Oak Ridge National Laboratory (ORNL), Technical Report, 2020

26. Hanson K, Sankar K M, Weck P F, Startt J K, Dingreville R, Deo C S, Sugar J D, Singh P M. Effect of excess Mg to control corrosion in molten $MgCl_2$ and KCl eutectic salt mixture. Corrosion Science, 2022, 194: 109914

27. Ding W, Shi H, Jianu A, Xiu Y, Bonk A, Weisenburger A, Bauer T. Molten chloride salts for next generation concentrated solar power plants: mitigation strategies against corrosion of structural materials. Solar Energy Materials and Solar Cells, 2019, 193: 298–313

28. Zhao Y, Vidal J. Potential scalability of a cost-effective purification method for $MgCl_2$-containing salts for next-generation concentrating solar power technologies. Solar Energy Materials and Solar Cells, 2020, 215: 110663

29. Gong Q, Shi H, Chai Y, Yu R, Weisenburger A, Wang D, Bonk A, Bauer T, Ding W. Molten chloride salt technology for next-generation CSP plants: compatibility of Fe-based alloys with purified molten $MgCl_2$–KCl–NaCl salt at 700 °C. Applied Energy, 2022, 324: 119708

30. Kurley J M, Halstenberg P W, McAlister A, Raiman S, Dai S, Mayes R T. Enabling chloride salts for thermal energy storage: implications of salt purity. RSC Advances, 2019, 9(44): 25602–25608

31. Ding W, Yang F, Bonk A, Bauer T. Molten chloride salts for high-temperature thermal energy storage: continuous electrolytic salt purification with two Mg-electrodes and alternating voltage for corrosion control. Solar Energy Materials and Solar Cells, 2021, 223: 110979

32. Ding W, Gomez-Vidal J, Bonk A, Bauer T. Molten chloride salts for next generation CSP plants: electrolytical salt purification for reducing corrosive impurity level. Solar Energy Materials and Solar Cells, 2019, 199: 8–15

33. Johnson T, Teats F, Pierce R D. A Method for the Purification of Molten Chloride Salts. Argonne National Laboratory (ANL), Technical Report, 1969

34. Zhang M, Ge J, Yin T, Zhang J. Redox potential measurements of Cr(II)/Cr Ni(II)/Ni and Mg(II)/Mg in molten $MgCl_2$–KCl–NaCl mixture. Journal of the Electrochemical Society, 2020, 167(11): 116505

35. Sun H, Zhang P, Wang J. Effects of alloying elements on the corrosion behavior of Ni-based alloys in molten NaCl–KCl–$MgCl_2$ salt at different temperatures. Corrosion Science, 2018, 143: 187–199

36. Ambrosek J W. Molten chloride salts for heat transfer in nuclear systems. Dissertation for the Doctoral Degree. Madison-Wisconsin: University of Wisconsin-Madison, 2011, 1–238

37. Kumar S, Wu C. Eliminating intermetallic compounds via Ni interlayer during friction stir welding of dissimilar Mg/Al alloys. Journal of Materials Research and Technology, 2021, 15: 4353–4369

38. Shah L H, Gerlich A, Zhou Y. Design guideline for intermetallic compound mitigation in Al–Mg dissimilar welding through addition of interlayer. International Journal of Advanced Manufacturing Technology, 2018, 94(5–8): 2667–2678

39. Varin R A, Czujko T, Mizera J. The effect of $MgNi_2$ intermetallic compound on nanostructurization and amorphization of Mg–Ni alloys processed by controlled mechanical milling. Journal of Alloys and Compounds, 2003, 354(1): 281–295

40. Elthalabawy W, Khan T. Liquid phase bonding of 316L stainless steel to AZ31 magnesium alloy. Journal of Materials Science and Technology, 2011, 27(1): 22–28

41. Wang S, Han W, Zhang M, Li M, Yang X, Sun Y. Electrochemical behaviour of magnesium(II) on Ni electrode in LiCl–KCl eutectic. Chemical Research in Chinese Universities, 2018, 34(1): 107–112

42. Zhu F. Microstructural evolution in austenitic stainless steels for extended-life power station applications. Dissertation for Doctoral Degree. Loughborough: Loughborough University, 2011, 1–173

43. Yamamoto Y, Brady M P, Lu Z P, Maziasz P J, Liu C T, Pint B A, More K L, Meyer H, Payzant E A. Creep-resistant, Al_2O_3-forming austenitic stainless steels. Science, 2007, 316(5823): 433–436

44. Endo H. The densities of magnesium at its melting point. Bulletin of the Chemical Society of Japan, 1927, 2(5): 131–134

45. McGonigal P J, Kirshenbaum A D, Grosse A V. The liquid temperature range, density, and critical constants of magnesium. Journal of Physical Chemistry, 1962, 66(4): 737–740

46. Wang X, Rincon J D, Li P, Zhao Y, Vidal J. Thermophysical properties experimentally tested for NaCl–KCl–$MgCl_2$ eutectic molten salt as a next-generation high-temperature heat transfer fluids in concentrated solar power systems. Journal of Solar Energy Engineering, 2021, 143(4): 041005–1, 041005–041008

47. Mezbahul-Islam M, Medraj M. A critical thermodynamic assessment of the Mg–Ni, Ni–Y binary and Mg–Ni–Y ternary

systems. Calphad, 2009, 33(3): 478–486

48. Ansara I, Dinsdale A, Rand M. Thermochemical database for light metal alloys. Office for Official Publications of the European Communities, 1998

49. Gong Q, Ding W, Chai Y, Bonk A, Steinbrecher J, Bauer T. Chemical analysis and electrochemical monitoring of extremely low-concentration corrosive impurity MgOHCl in molten MgCl$_2$–KCl–NaCl. Frontiers in Energy Research, 2022, 10: 811832

50. Robb K, Baird S, Massengale J, Hoyt N, Guo J, Moore C. Engineering-Scale Batch Purification of Ternary MgCl$_2$–KCl–NaCl Salt Using Thermal and Magnesium Contact Treatment. Oak Ridge National Lab. (ORNL), Technical Report, 2022